

# Boosting the electrochemical characteristics of nickel-iron cyano-bridging metal organic framework via thermal curing for developing supercapacitor and electrocatalyst platforms

Khaled G. Mahmoud, Farouk A. Rashwan, Hussein M. El-Sagher, Mohamed Khairy\*

Chemistry Department, Faculty of Science, Sohag University 82524, Egypt

Received: 7 Jul. 2022, Revised: 1 Aug. 2022, Accepted: 2 Aug. 2022.

Published online: 1 Sept. 2022

**Abstract:** Cyano-bridging metal organic frameworks or Prussian blue analogues (PBA) have attracted much attention for developing electrochemical-based devices because of large surface area, stability, conductivity and interesting redox features. Herein, nickel-iron cyano-bridging metal framework (NICF) was prepared by a simple co-precipitation method, calcined at high temperatures and the utilized for electrochemical applications. Nano-sized nickel-iron cyano-bridging metal framework with a large surface-area and pure cubic crystal was obtained. The NICF was calcined at different temperatures (100, 200, 300, 400 and 500 °C) then the electrochemical properties were studied by simple drop cast on a glassy carbon electrode (GCE). Interestingly, the S100/GCE platform (for NICF sample calcined at 100 °C) showed a superior specific capacitance ( $C_s$ ) of 571 F/g compared to 428 F/g for NICF/GCE in 0.1M KOH. While, the S200/GCE (for NICF calcined at 200 °C) exhibited a low overpotential ( $\eta$ ) of 450 mV toward oxygen evolution reaction (OER) compared to 1.0 V and 1.3 V for as-prepared NICF modified GCE and unmodified GCE, respectively to deliver a current density of 10 mA/cm<sup>2</sup> in 1.0 M KOH. Based on these results, it was found the thermal curing of NICF at relatively high temperature could be used as a simple approach for boosting the electrochemical features of PBA leading to design efficient and low-cost electrochemical-based devices.

**Keywords:** Prussian blue analogues, Supercapacitor, Vacancies, Oxygen evolution reaction, Electrocatalyst.

## 1 Introduction

To fulfill the rising demand for energy internationally and develop clean sources of energy to combat climate change, renewable energy harvesting, and storage are significant challenges that have drawn great research in recent decades. Thus, the researchers have devoted great efforts to exploit renewable and clean energy sources. Besides, courage steps have been taken to get rid of fossil fuel dependence and environmental wasting energies. For example, German government has been closed three nuclear reactors in the beginning of 2022 year. Further, large number of hybrid vehicles has been produced. However, the technical efficiency for energy conversion and storage is still limited because of the lack of promising materials. Thus, looking for new materials that are able to store or generate energy from renewable resources with high capability and reliability are urgently required. Among the various materials, Prussian blue (PB) and its analogues (PBAs) are considered as excellent candidates for developing electrochemical devices due to their interesting characteristics in terms of large number of active sites, high surface area, and open porous network. PB and PBAs have

been reported extensively as electrode material for lithium-, sodium-, and potassium-ions batteries [1,2] and supercapacitors [3-5]. Further, they have been also utilized as precursors for preparation of new materials used in construction of metal-air batteries and fuel cells [6, 7].

The chemical formula of PB or PBA are  $AM[M(CN)_6].nH_2O$ , where (A= alkali metals e.g.  $K^+$ ,  $Na^+$ , ... , and M, M= transition metal e.g.  $Ni^{2+}$ ,  $Mn^{2+}$ ,  $Fe^{3+}$  or  $Fe^{2+}$ ,  $Co^{2+}$ , ... etc.). Such formula enables synthesis of variety coordination polymers of transition metals with multifunctionality. It divided into two major categories water soluble Prussian blue (WSPB) and water insoluble Prussian blue (WIPB). The WSPB has been used intensively for energy storage applications in non-aqueous alkali ions batteries. Wu, *et al.* prepared PB with a chemical formula of  $K_{1.68}Fe_{1.09}Fe(CN)_6 \cdot 2.1H_2O$  as cathode material for non-aqueous potassium-ion battery. It offered a specific capacity of 110 mA h g<sup>-1</sup> [8]. Wheeler, *et al.* synthesized a low-potential PBA for sodium-ion batteries (MnHCF [9] which exhibited a reversible sodium insertion at -0.86 V vs. SHE and maintained the structure characteristic even after multiple charge/discharge cycles.

\* Corresponding author E-mail: [mohamed.khairy@science.sohag.edu.eg](mailto:mohamed.khairy@science.sohag.edu.eg)

On the other hand, WIPB does not contain any alkali metal ions in its chemical structure. It also utilized numerous for energy storage applications. *Khairy, et al.* prepared nanosized NiHCF modified screen-printed electrodes as a flexible superbattery platform which acts as a battery in neutral medium of potassium chloride and supercapacitor in basic medium of potassium hydroxide [10]. Moreover, PB and PBAs with cubic crystals have been exploited as precursor material for preparation metal oxides, and sulfides [11-13] *Mule, et al* prepared hollow structured  $\text{Co}_3\text{S}_4/\text{CuS}_2/\text{NiS}_2$  utilizing sulfur vapor reaction with potassium hexacyanocobaltate (PHCCo), (PHC Cu) or (PHCNi) under inert atmosphere. The resulting nanocubes metal sulfides were used for battery-type electrode material for hybrid supercapacitors (SCs) [14]. Further, there are several strategies for tuning the PB and its analogous structures by creating  $[\text{Fe}(\text{CN})_6]$  or CN vacancies. Performing unconventional CN vacancies within the crystals has been occurred *via* plasma bombardment as reported by *Yu, et al.* Such unconventional CN vacancy suppressed iron-leaching in NICF pre-catalyst for overpotential enhancement of oxygen evolution reaction (OER) [15]. *Simonov, et al.* report a hidden diversity CN vacancy networks in PBAs and represent corresponding application as electrode material for batteries [16].

In the present manuscript, we report a facile co-precipitation method for synthesis of large surface area NICF with nanosized dimensions of 35 nm and aggregated at higher temperatures. The NICF was calcined at different temperatures (100, 200, 300, and 400 °C). The prepared NICF and its derivatives samples were explored for construction of the supercapacitor and electrocatalytic applications. It was found crystal structure; surface area and number of active sites could be significant key factors for boosting the electrochemical characteristics.

## 2 Materials and method

### 2.1. Chemicals

All chemicals are of the highest analytical grade and used without further purification. Nickel (II) nitrate hexahydrate ( $\text{Ni}(\text{NO}_3)_2 \cdot 6\text{H}_2\text{O}$ ), polyvinylpyrrolidone (PVP), trisodium citrate dihydrate (SC), potassium hexacyanoferrate(III) (PHCF,  $\text{K}_3[\text{Fe}(\text{CN})_6]$ ), polytetrafluoroethylene (PTFE), carbon black, potassium hydroxide (KOH) and ethanol absolute were purchased from Sigma-Aldrich Co. LTD. All the solutions were prepared by doubly distilled water with a specific resistance  $\geq 18 \text{ M}\Omega \text{ cm}$ .

### 2.2. Synthesis of nickel-iron cyano-bridging metal organic frameworks and its derivatives.

The NICF sample was synthesized by dissolving of 150 mg SC, 300 mg PVP, and 175 mg  $\text{Ni}(\text{NO}_3)_2 \cdot 6\text{H}_2\text{O}$  in 20 mL doubly distilled water. The mixture was stirred for 15 minutes. A 20 mL of PHCF solution containing 132 mg was

added to the above mixture dropwise and stirred for one-hour. The final mixture was aged for 24.0 hours at room temperature. The precipitate was separated by a centrifuge at high-speed rotor of 10,000 rpm for 20 min. To remove residual PVP and SC, the precipitate was washed several times by water/ethanol mixture and dried at 50 °C. Then, the NICF was calcinated at 100 °C, 200 °C, 300 °C, and 400 °C for 2.0 hours in a muffle furnace with a heating rate of 2.0 °C/minute to obtain S100 S200, S300 and S400 samples, respectively. The NICF derivatives left to cool at room temperature before further test experiments.

### 2.3. Electrode and Electrochemical cell construction.

Three-electrode configuration cell consists of GCE modified with NICF or its derivatives as working electrode, platinum (Pt) wire as counter electrode and Hg/HgO as reference electrodes. The surface area of GCE is  $0.07 \text{ cm}^2$ . A suspension solution of NICF was prepared by mixing 80% of NICF (2.5 mg/5.0 mL) or its derivatives with 10% carbon black and 10 % PTFE. A 5  $\mu\text{L}$  of NICF or its derivatives forms suspension drop casted on the GC electrode and left to dry for 30 minutes in electric furnace at temperature 50 °C result in mass load about 2.0  $\mu\text{g}$  of active material with a real load about  $30 \mu\text{g cm}^{-2}$ .

### 2.4. Characterization of NICF and its derivatives.

The morphology of NICF and calcinated forms was investigated using Field emission scanning electron microscopy (ZEISS model Sigma 500). The samples were well grinded and fixed onto a specimen of double-sided carbon tape. To increase the surface conductivity, a 10 nm Pt film deposited *via* ion sputtering at room temperature to obtain high-resolution images. The SEM operated at 30 kV to obtain high-resolution images. Further, transmission electron microscopy (TEM) images carried out at a JEOL JEM model 2100F microscope. The TEM operated at an acceleration voltage of 200 kV to obtain a lattice resolution of 0.1 nm. The NICF or its derivatives sample were dispersed in ethanol solution using an ultrasonic cleaner and then introduced onto a copper grid. Prior to inserting the samples into the TEM column, the grid was dried for 10 minutes in vacuum.

The thermal gravimetric analysis of NICF was measured by using TG-60, Shimadzu Ltd, Japan under a flow of air. Wide-angle powder X-ray diffraction (XRD) performed using X-ray diffractometer, model D8-Advance with monochromatic  $\text{CuK}_\alpha$  radiation ( $\lambda = 1.54 \text{ \AA}$ ). The XRD patterns were measured *in 2\theta* range of  $10^\circ$  to  $80^\circ$  by employing a scanning rate of  $0.06 \text{ min}^{-1}$ . The diffraction data are analyzed using the DIFRAC plus Evaluation Package (EVA) software with the PDF-2 Release 2009. Fourier transform infrared spectroscopy (FTIR) carried out on Bruker ALPHA II compact FTIR spectrometer set at 24 scan with resolution  $4 \text{ cm}^{-1}$ . The FTIR spectra of the NICF samples were recorded in range from 400 to  $4000 \text{ cm}^{-1}$ .

The surface textural properties of NICF and its derivatives were analyzed by measurement of nitrogen

adsorption/desorption isotherm using BELSORP mini-analyzer, BEL Co., JP Ltd at 77 K. The specific surface area ( $S_{BET}$ ) was estimated by using Brunauer–Emmett–Teller (BET) method with multipoint adsorption data from the linear segment of the nitrogen adsorption isotherm curve.

The electrochemical experiments were performed using IVIUM Compact Stat.h potentiostat/galvanostat workstation controlled by IVIUM software, cyclic voltammetry (CV), linear sweep voltammetry (LSV), galvanic charge/discharge (GCD) and chronoamperometry (CA), techniques were carried out at room temperature. The specific capacitance ( $C_s$ ) was calculated from the CV curves by equation (1)

$$C_s = \frac{1}{vm(\Delta V)} \int_{v_1}^{v_2} i V dV \quad (1)$$

Or, from the GCD curves by the following equation (2)

$$C_s = \frac{It}{m(\Delta V)} \quad (2)$$

Where,  $C_s$  is specific capacitance in F/g,  $v$  is the potential scan rate in V/s,  $\Delta V$  is the potential window between  $V_1$  and  $V_2$ ,  $m$  is the mass loading of active species,  $\Delta t$  is the discharge time in seconds and  $I$  is the applied discharge current in Ampere.

### 3 Results and discussion

#### 3.1. Characterization of NICF sample and its derivatives

A co-precipitation method was used for large-scale synthesis of NICF sample by reaction between  $Ni^{2+}$  ions and  $[Fe(CN)_6]^{3-}$  in the presence of citrate anions and PVP as structure directing agent. The concentration of citrate anions could control the growth rate of NICF particles as reported previously [17]. The PVP solution surrounds the formed particle to prevent the co-aggregation of the small particles. The NICF with a chemical formula of  $Ni_3[Fe(CN)_6]_2 \cdot nH_2O$  was formed (Inset Fig. 1A). Upon thermal treatment, the amount of hydrated water subsequently affects the NICF crystal. The TGA analysis provides amazing insight regarding to thermal stability of the materials [18]. Figure 1 represents the TGA curve of as-prepared NICF in air atmosphere. Upon heating treatment, the hydrated water evaporated at 100 °C *via* weight loss of 7.5% followed by losing of crystalline water molecules with weight loss of 29.3% at 200 °C. Deformation of NICF crystal takes place at higher than 200 °C with creation of vacancies leading to amorphization. The nickel nitride and iron carbide compounds were formed at higher than 300 °C and weight loss of 44.8%. Finally, NiFe alloy was created at higher than 400 °C [10]. These data confirmed by measuring of the surface area, crystallinity, and functionality of NICF as shown in Figure 1B and Figure 2.

The surface area of NICF and its derivatives was measured by utilizing  $N_2$  adsorption/desorption isotherm

curves as shown in Figure 1B. Type IV isotherms with a H2-type hysteresis loop were represented indicating formation of mesoporous framework within NICF or its derivatives. The specific surface areas were calculated and found to be 452, 390.8, 133.7, 56.5  $m^2g^{-1}$  for NICF, S100, S200 and S300, respectively. It well known that, the PB and PBA offered large open porous network forming large surface area that might relate to interconnection between the NICF crystals. It was found the surface area of NICF decrease with raising the calcination temperatures. This result indicates crystal structure deformation that reduces interstitial mesopores and cavities.

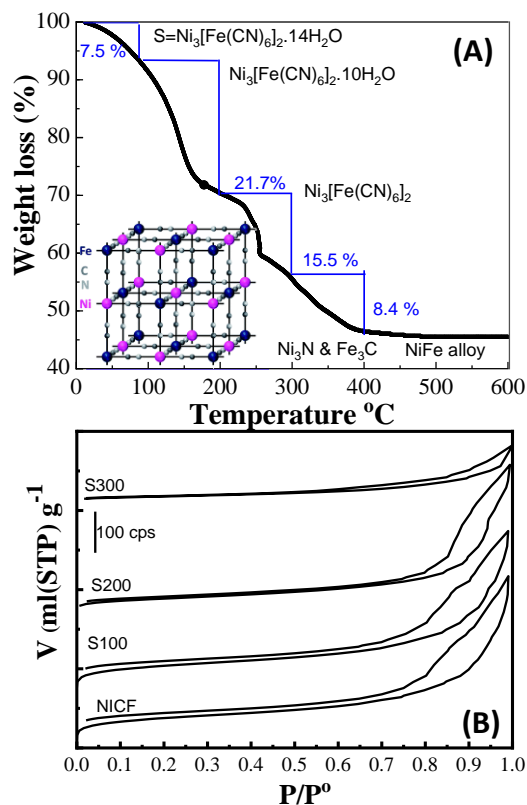


**Figure 1.** (A) Thermogravimetric analysis (TGA) of NICF under air flow, (B)  $N_2$  adsorption/desorption isotherms of NICF, S100, S200, and S300 respectively.

The crystal structure of NICF and its calcined derivatives were investigated by wide-angle X-ray diffraction (XRD) as shown in Figure 2A. Well-resolved and distinctive diffraction peaks of NICF are located at  $2\theta^\circ$  of 15.01°, 17.3°, 24.54°, 29.1°, 30.64°, 35.1°, 39.41°, 43.4°, 50.65°, 53.89°, 57.13°, 66.08°, and 68.87°. These diffraction peaks can be indexed for (111), (200), (220), (311), (400), (420), (422), (440), (600), (620), (640) and (642), respectively, consistent with JCPDS no. 46-0906 for  $Ni_3[Fe(CN)_6]_2 \cdot 10H_2O$ . The NICF showed a cubic ( $F\bar{4}3m$ ) symmetry with a lattice constant of  $a = 10.22 \text{ \AA}$ . These diffraction peaks did not change upon heating at 100 °C revealed stability of NICF crystal and losing only the hydrated water. At 200 °C, all the diffraction peaks were

decreased significantly indicating deformation of the NICF crystals. After 300 °C, The XRD of NICF was changed due to decomposition of NICF crystals and formation of nickel nitride and iron carbide compounds. The crystal size of NICF and its derivatives were calculated and depicted inset Figure 2A using Scherrer's Equation [19] as following.

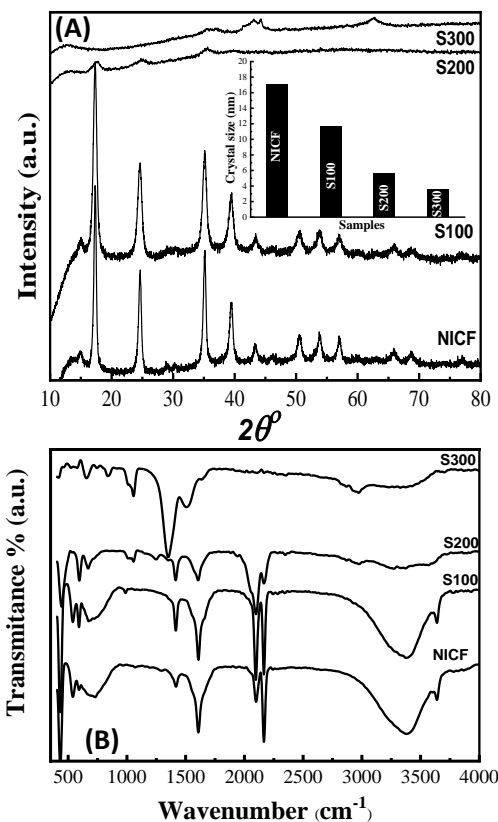
$$ls = \frac{0.92 \lambda}{\beta \cos(\theta)} \quad (3)$$

Where  $ls$  is the crystal size,  $\beta$  is the full wave half maximum (FWHM),  $\theta$  is the incident beam angle. It was found the crystal size decreases consequently upon increasing calcination temperatures, which indicates shrinking of NICF crystals. These results are consistent with TGA analysis in Figure 1A. Besides, the pore sizes were decreased as shown in N<sub>2</sub> adsorption/desorption isotherm (Figure 1B) leading to formation of amorphous phase of NICF combined with the crystalline one at 200 °C. Thus, the active sites might be changed.

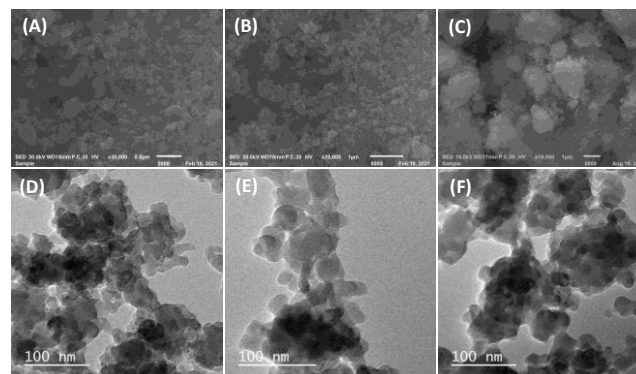
The functionality of NICF and its derivatives were also investigated using the FTIR spectroscopy as shown in Figure 2B. Two small absorption bands at 3708 and 3649 cm<sup>-1</sup> assign to symmetric and asymmetric stretching of H<sub>2</sub>O molecules, respectively. The broad absorption band at 3375 cm<sup>-1</sup> attribute to O-H stretching. These results indicate the presence of hydrated and coordinated water molecules in NICF sample as shown in TGA curves. Another absorption band at 1610 cm<sup>-1</sup> attributes to O-H bending.[20] The broad absorption bands at 2973 – 2865 cm<sup>-1</sup> assign to –CH<sub>2</sub> antisymmetric and symmetric stretching, respectively, indicating the presence of residual PVP. The absorption peaks at 2169 and 2091 cm<sup>-1</sup> attribute to C≡N bridging stretching, respectively. When CN group forms a complex with transition metals tends to act as  $\sigma$  donor and the complex depends upon the electronegativity, oxidation state and coordination number of the bonded metal. Thus, the absorption band at 2169 and 2091 cm<sup>-1</sup> might be related to Ni(II)C≡N-Fe(II) and Ni(II)-C≡N-Fe(III) indicating the presence of Fe(II)/Fe(III). As well as, the starting precursor include Fe<sup>3+</sup>, species in the NICF framework as suggested previously [21, 22]. These peaks disappeared after heating over 300 °C. The small absorption bands at 1414 and 1346 cm<sup>-1</sup> assign to symmetric –COO<sup>-</sup> stretching and -CH deformation which regarding to residual citrate ions. The broad peak from 1003 cm<sup>-1</sup> to 1061 cm<sup>-1</sup> attribute to –C-C- stretching. The absorption bands at 591.5 and 434.6 cm<sup>-1</sup> can be assigned to Fe-CN bending and Fe-CN stretching vibration modes, respectively. The absorption peak at 542.5 attributes to Ni-NC stretching. Upon thermal treatment absorption peak intensity related to CN- group was changed at after 100 °C, indicate the presence of oxygen might changes Ni(II)C≡N-Fe(II) and Ni(II)-C≡N-Fe(III) [15]. The variation in the crystal structure, surface area, and chemical compositions of NICF derivatives will be very interesting for electrochemical applications.

Figure 3 shows scanning electron microscopy images and transmission electron micrographs of NICF and its

derivatives that reveal a spherical nanoparticle with an average size of 35 nm even after calcination. After calcination at 200 °C, the nanoparticles were aggregated. The TEM micrographs showed aggregated spherical nanoparticles with an average size of 35 nm ± 5 nm. It is observed dark and bright areas between the interconnected particles with smoothed surfaces, indicating the formation of porous network. Further, different crystalline domains with discontinuous atomic arrangements distinguished in a dark color, might suggest the amorphization of NIFC crystal at high temperatures [10]. Such open porous network is a significant key feature for enhancing the applicability of NICF in electrochemical devices.



**Figure 2.** (A) FT-IR and (B) XRD of NICF and its derivatives (inset calculated crystal size of NICF and its derivatives based on XRD analysis).



**Figure 3.** Scanning electron microscopy (SEM) images and transmission electron microscopy micrographs of (A, and D) NICF, (B, and E) S100, and (C, and F) S200.

### 3.2. Electrochemical applications

#### 3.2.1. Design of energy storage device

The electrochemical behavior of NICF and its derivatives were studied by cyclic voltammetry and galvanostatic charge/discharge in 0.1M KOH. Figure 4 shows the CV curves of NICF and its derivatives at different scan rates from 20-200 mV/s in 0.1 M KOH. The CV curves revealed one redox wave at anodic peak potential of 0.9 V and cathodic peak potential of 0.51 V vs. Hg/HgO at a scan rate of 20 mV/s. Further, the anodic peak potential is shifted to more positive values and cathodic peak potential is shifted to more negative values with increasing potential scan rates. Thus, it is clear the electrochemical behavior of NICF materials are belongs to quasi-reversible process because due to the presence of reverse wave and the peak potential separation ( $\Delta E_p$ ) exceed 59 mV for one-electron transfer process. The peak currents were increased with increasing the scan rate from 20 to 200 mV/s. It is observed that, the peak current is correlated linearly with square root of scan rates, indicating the majority of diffusion-controlled process as shown in Figure 5. Among the prepared samples, S100 showed the highest peak current. Thus, the sample S100 will be promising for energy storage applications by utilizing S00/GCE battery-like electrode.

To investigate the storage mechanism, the contributions of diffusional and surface processes at NICF were studied. The concrete fraction of the diffusion and surface processes can be deduced through the Dunn's Equation, Equation (4) at low scan rates from 1 to 10 mV/s [23, 24].

$$i(V)/v^{1/2} = k_1 v^{1/2} + k_2 \quad (4)$$

Where the surface-controlled part ( $k_1 v$ ) and the diffusion-controlled part of  $k_2 v^{1/2}$  can be quantified. The fraction of surface and diffusion-controlled contributions were calculated to be 16.48% and 83.16% of the total stored charge in 0.1 M KOH. Thus, the energy storage mechanism is mainly attributed to the quasi-reversible reaction of  $\text{Ni}^{\text{II}}/\text{Ni}^{\text{III}}$  [25].

Figure 6A shows the galvanostatic charge/discharge curves of NICF derivatives at 5A/g in 0.1 M KOH. It is observed a discharge plateau at 0.75 V, suggesting battery-like electrodes was formed in case of NICF and its derivatives. Among the NICF derivatives, the sample S100 represents the most promising electrode material with long discharge time. The specific capacitance (SC) of NICF estimated to be 428 F/g, increased to 570 F/g after thermal treatment at 100 °C and then decreased at 200 °C (321 F/g) and 300 °C (36 F/g). The high SC of NICF might be attributed to capacitive behavior *via* large surface area compared to the published literatures [15, 16]. We can see enhancement in the specific capacitance value after thermal treatment at 100 °C although it showed a lower surface area compared to the as-prepared NICF. This interesting

behavior is might due to increasing of the surface-active sites that facilitate the conversion of  $\text{Ni}^{2+}/\text{Ni}^{3+}$  *via* losing of the hydrated water molecules in NICF material and increasing the intercalated space to guest more ions. Besides, the reduction of the specific capacitances at 200 °C and 300 °C is regarding to the reduction of their surface area (i.e. 133, and 56.5 m<sup>2</sup>/g).

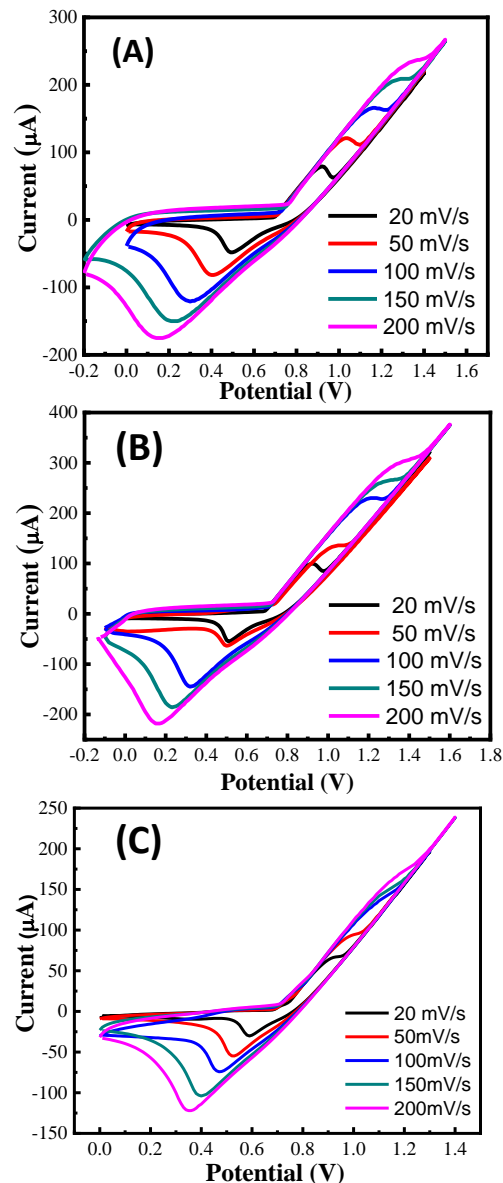


**Figure 4.** Cyclic voltamograms of (A) NICF, (B) S100, and (C) S200 s at different scan rate respectively.

The supercapacitive performance of NICF calcined at 100 °C was tested at different charging/discharging currents as show in Figure 6B. The estimated values of specific capacitances ( $C_s$ ) are calculated from the discharge curves (Equation 2) and found to be 570, 516, 513, 460 and 440 F/g at 5, 4, 3, 2 and 1 A/g, respectively. Small variation of  $C_s$  upon charging at various currents beside discharge plateau at 0.7 ~ 0.6 V, indicate the battery-like with high

capability performance. To investigate the stability of GC/NICF, multi-consecutive charge /discharge cycles were carried out (Fig. 6C). Excellent stability performance with stable discharge currents compared to previously reported Prussian blue analogues was presented which confirm the promising stability of NICF/GC platform for supercapacitor applications [26]

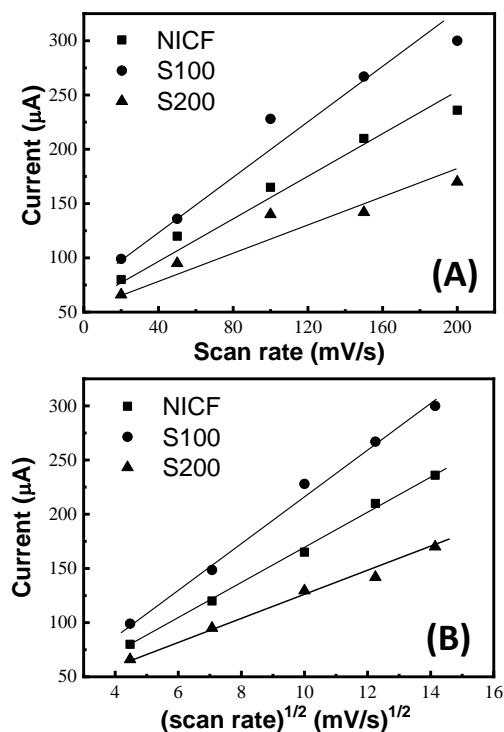


**Figure 5.** Variations of the peak current of NICF derivatives with (A) potential scan rates, (B) Square root scan rates.

### 3.2.2. Design of electrocatalyst for oxygen evolution reaction

The electrochemical behavior of NICF and its derivatives modified glassy carbon electrode (GC) are studied in 1.0 M KOH by linear sweep voltammetry (LSV) technique in the potential range of 1.3 to 1.9 V *vs.* RHE at a scan rate of 5 mV/s Figure 7A. The LSV curves moves to Y-axis with increasing the temperatures until 200 °C. The modified electrode by S200 delivers a current density of 10 mA/cm<sup>2</sup> at overpotential of 450 mV. The oxidation peak at 1.45 V *vs.* RHE corresponding to oxidation of Ni(II) to Ni(III) [15, 16, 25]. Figure 7B shows the Tafel slopes of GC/NICF and GC/S200 and found to be 635 and 176 mV/dec with regression coefficients ( $R^2$ ) of 0.969, and 0.999, respectively. Thus, the thermal treatment of NICF up to 200 °C facilitates the oxygen evolution reaction (OER). This significant enhancement is attributed to crystal lattice deformation of NICF upon heating leading to amorphization as shown in XRD and FTIR. It was found, the crystal deformation increased the number of active sites, altered the electron transfer mobility and caused the oxidation of hydroxyl groups more easier in 1.0 M KOH [27]. It is observed that, the S100 has a weak electrocatalytic activity

toward OER, which indicate no contributions of hydrated water or crystalline water in OER enhancement. At higher than 300 °C, the electrocatalytic activity of the NICF derivatives were decreased toward OER. This, result indicates that the crystallinity limit of NICF is a significant key factor in the OER. Thus, a simple strategy for controlling the crystal deformation of NICF and its electrocatalytic efficiency was investigated for the first time. To check the electrochemical stability of GC/S200 for OER, a chronoamperometry measurement was employed as shown in Figure 7C at a applied potential of 1.7 *vs.* RHE. We can see a stable chronoamperogram of GC/S200 in 1.0 M KOH for one hour at a constant current density of 10 mA/cm<sup>2</sup>, indicating high stability of S200 for oxygen evolution reaction.

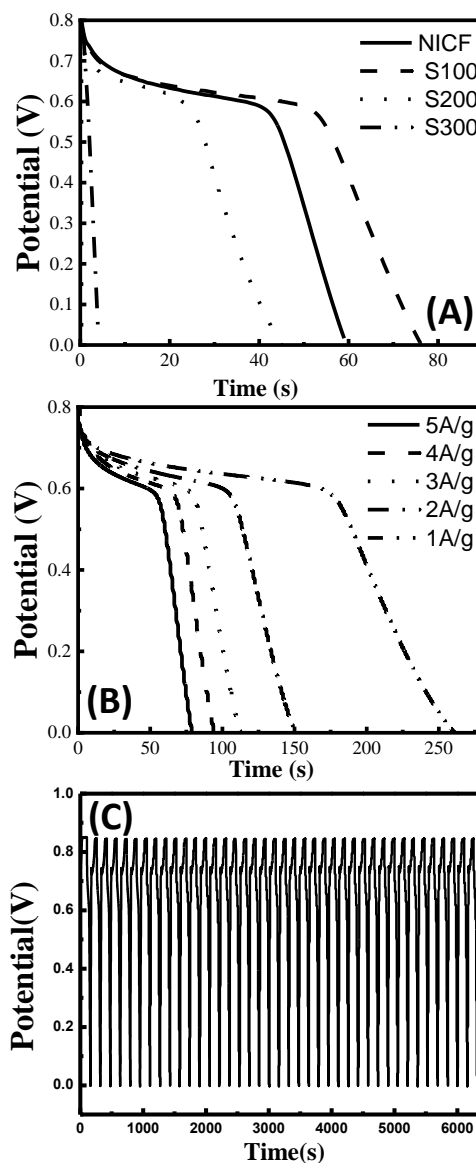


**Figure 6.** (A) Discharge curves of NICF and its derivatives at 5A/g in 0.1 M KOH, (B) galvanostatic discharge curves of S100 at different discharging currents density, (C) Multi-charge/discharge cycles of S100 at 5A/g.

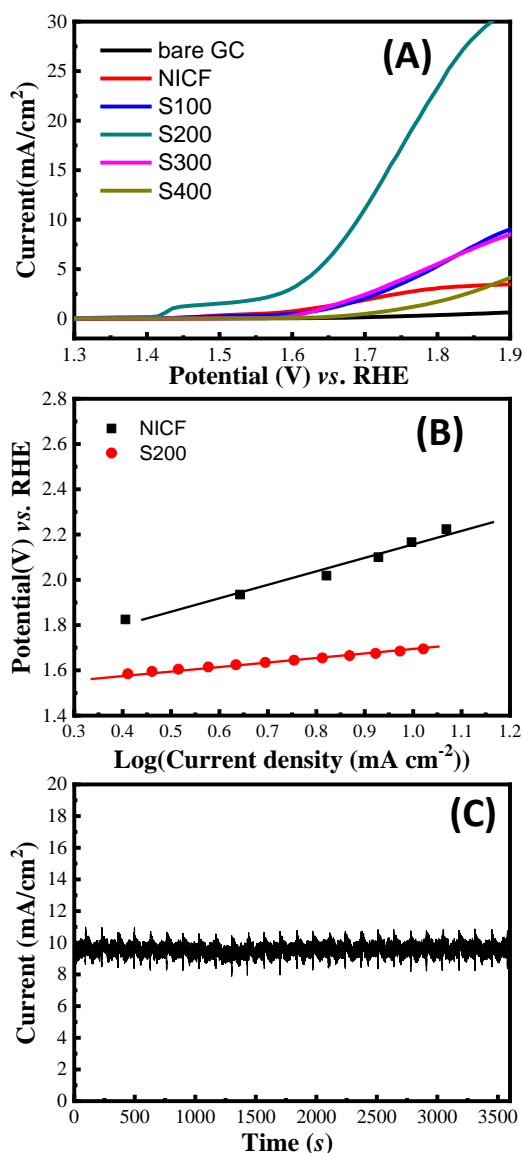


**Figure 7.** (A) Linear sweep voltammetry curve of NICKF and its derivatives modified GCE at 5.0 mV/s in 1.0 M KOH, (B) Tafel slopes of NiHCF and S200 samples, (C) Chronoamperometry measurement curve of sample S200 at 1.7 V for one hour in 1M KOH.

## 4 Conclusion

PBAs have attracting much interest due to its promising electrochemical characteristic, which offer construction of efficient nanodevices. In the present manuscript, we report a facile co-precipitation method for fabrication of nanostructured NICKF with large surface area of 450 m<sup>2</sup>/g and average particle size around 35 nm. The as-synthesized NICKF was thermally treated at different temperatures in the range 100 °C to 400 °C. Then, the prepared samples were investigated for design new platforms for energy storage and conversion. Interestingly, the NICKF sample calcined at 100 °C showed promising supercapacitive behavior with a

specific capacitance of 570 F/g. While, the NICKF sample calcined at 200 °C represented high electrochemical activity for OER with  $\eta_{10} = 450$  mV. This result revealed that, extent of crystallinity is a significant key factor for boosting the electrochemical applicability of NICKF in addition to surface area and functionality. Further, a simple thermal treatment approach for controlling the crystal deformation of NICKF was reported for the first time compared to previously sophisticated methods in literatures.

## 5 References

- [1] W.J. Li, C. Han, G. Cheng, S.L. Chou, H.K. Liu, S.X. Dou, *Small*, 15 (2019) 1900470.
- [2] P. Nie, L. Shen, H. Luo, B. Ding, G. Xu, J. Wang, X. Zhang, *Journal of Materials Chemistry A*, 2 (2014) 5852-5857.
- [3] E.S. Goda, S. Lee, M. Sohail, K.R. Yoon, *Journal of Energy Chemistry*, 50 (2020) 206-229.
- [4] P. Díaz, Z. González, R. Santamaría, M. Granda, R. Menéndez, C. Blanco, *Electrochimica Acta*, 212 (2016) 848-855.
- [5] Y. Lin, L. Zhang, Y. Xiong, T. Wei, Z. Fan, *Energy & Environmental Materials*, 3 (2020) 323-345.
- [6] H. Yi, R. Qin, S. Ding, Y. Wang, S. Li, Q. Zhao, F. Pan, *Advanced Functional Materials*, 31 (2021) 2006970.
- [7] Y. Yang, Y. Xue, H. Zhang, H. Chang, *Chemical Engineering Journal*, 369 (2019) 813-817.
- [8] X. Wu, Z. Jian, Z. Li, X. Ji, *Electrochemistry Communications*, 77 (2017) 54-57.
- [9] S. Wheeler, I. Capone, S. Day, C. Tang, M. Pasta, *Chemistry of Materials*, 31 (2019) 2619-2626.
- [10] M. Khairy, K.G. Mahmoud, F.A. Rashwan, H.M. El-Sagher, C.E. Banks, *Journal of Energy Storage*, 46 (2022) 103872.
- [11] C. Xuan, J. Zhang, J. Wang, D. Wang, *Chemistry—An Asian Journal*, 15 (2020) 958-972.
- [12] B. Singh, A. Indra, *Materials Today Energy*, 16 (2020) 100404.
- [13] J. Wang, B. Wang, X. Liu, J. Bai, H. Wang, G. Wang, *Chemical Engineering Journal*, 382 (2020) 123050.
- [14] A.R. Mule, B. Ramulu, J.S. Yu, *Small*, 18 (2022) 2105185.
- [15] Z.-Y. Yu, Y. Duan, J.-D. Liu, Y. Chen, X.-K. Liu, W. Liu, T. Ma, Y. Li, X.-S. Zheng, T. Yao, *Nature communications*, 10 (2019) 1-9.
- [16] A. Simonov, T. De Baerdemaeker, H.L. Boström, M.L. Rios Gomez, H.J. Gray, D. Chernyshov, A. Bosak, H.-B. Bürgi, A.L. Goodwin, *Nature*, 578 (2020) 256-260.

- [17] Y.D. Chiang, M. Hu, Y. Kamachi, S. Ishihara, K. Takai, Y. Tsujimoto, K. Ariga, K.C.W. Wu, Y. Yamauchi, *European Journal of Inorganic Chemistry*, 2013 (2013) 3141-3145.
- [18] D. Domonov, S. Pechenyuk, Y.P. Semushina, *Journal of Thermal Analysis and Calorimetry*, 146 (2021) 629-635.
- [19] A. Monshi, M.R. Foroughi, M.R. Monshi, *World J Nano Sci Eng*, 2012, 2: 154, 160 (2012).
- [20] B.M. Cullum, T. Vo-Dinh, *Handbook of Spectroscopy*, 2 (2003) 1.
- [21] X. He, L. Tian, M. Qiao, J. Zhang, W. Geng, Q. Zhang, *Journal of Materials Chemistry A*, 7 (2019) 11478-11486.
- [22] J. Li, L. He, J. Jiang, Z. Xu, M. Liu, X. Liu, H. Tong, Z. Liu, D. Qian, *Electrochimica Acta*, 353 (2020) 136579.
- [23] K. Wang, Q. Li, Z. Ren, C. Li, Y. Chu, Z. Wang, M. Zhang, H. Wu, Q. Zhang, *Small*, 16 (2020) 2001987.
- [24] K. Wang, R. Bi, M. Huang, B. Lv, H. Wang, C. Li, H. Wu, Q. Zhang, *Inorganic Chemistry*, 59 (2020) 6808-6814.
- [25] R. Ojani, J.-B. Raoof, S.R.H. Zavvarmahalleh, *Electrochimica Acta*, 53 (2008) 2402-2407.
- [26] M. Khalid, A.M. Honorato, *Journal of energy chemistry*, 27 (2018) 866-873.
- [27] J.A.D. del Rosario, G. Li, M.F.M. Labata, J.D. Ocon, P.-Y.A. Chuang, *Applied Catalysis B: Environmental*, 288 (2021) 119981.